SEMARAK ILMU PUBLISHING

CFD Letters

Journal homepage:
https://semarakilmu.com.my/journals/index.php/CFD_Letters/index
ISSN: 2180-1363

Effect of Chamfered Turbulators on Performance of Solar Air Heater - Numerical Study

Arunkumar Honnesara Sheshadri[1], Madhwesh Nagaraja[1*], Anirudh Hegde K[1], Manjunath Mallashetty Shivamallaiah[2], Kota Vasudeva Karanth[1], Younes Amini[3]

[1] Department of Mechanical and Industrial Engineering, Manipal Institute of Technology, Manipal Academy of Higher Education, Manipal - 576104, Karnataka, India
[2] Department of Mechanical and Manufacturing Engineering, Manipal Institute of Technology Bengaluru, Manipal Academy of Higher Education, Manipal, Karnataka, India
[3] Nuclear Fuel Cycle Research School, Nuclear Science and Technology Research Institute, Tehran, Iran

ARTICLE INFO

Article history:
Received 20 November 2023
Received in revised form 21 December 2023
Accepted 18 January 2024
Available online 30 June 2024

Keywords:
Solar air heater; Turbulence; Thermal enhancement factor; Chamfer turbulator

ABSTRACT

This paper presents a numerical analysis of the thermal performance improvement in a flat plate solar air heater equipped with chamfered turbulators attached below the absorber plate for evaluating performance for Reynolds numbers ranging from 3,000 to 21,000. According to the research, chamfered turbulators caused the flow to become highly turbulent. This flow behaviour with flow separation around the turbulators positively affects performance. This paper attempts to explain the complex flow behaviour found during the analysis. The turbulator diameter varies in 1 mm increments from 3 to 7 mm at a constant longitudinal pitch of 200 mm. The number of turbulator rows in the transverse direction is kept constant at three. The chamfer is represented by the flow attack angle, which can be 30°, 45°, or 60° facing the direction of flow and opposing the direction of flow. The results showed that a 7mm diameter turbulator with a 30° chamfer angle placed against the flow of air yielded a considerably more significant thermal enhancement factor of 1.15 over the spectrum of flow Reynolds number studied.

1. Introduction

Energy security is critical to the future energy policy of every country. Those countries with an excess of energy or a steady supply of energy in the following years will be able to maintain or grow their power and influence over the global economy. In the future, fuels such as petrol and diesel may be worth more than gold. Renewable energy, such as solar energy, is far superior for long-term development. Unlike fossil fuels, which run out of energy quickly, the sun produces more than enough energy to supply the demands of the entire planet. The only obstacle is our ability to efficiently and economically transform solar energy into usable form. Flat plate SAH has been used for applications requiring heated air or water at moderate temperatures. SAH absorber plate is

* *Corresponding author.*
E-mail address: madhwesh.n@manipal.edu (Madhwesh N.)

https://doi.org/10.37934/cfdl.16.11.1736

required to transfer the maximum heat absorbed by the working fluid with greater efficiency. In this aspect, many design and operating criteria influence the thermal efficiency of a solar air heater.

The computational tool is most effective in optimizing the design of the heat exchangers, especially in solar applications like solar still [1], solar water heaters [2], solar PV panels [3], Solar Air Heater (SAH) [4], Solar drying chamber [5], Rheological Behaviour of the Solar Collector [6] etc. Various researchers have carried out the CFD analysis to optimize the SAH design to enhance the heat transmission rates in the SAH. Researchers have explored various types of turbulators, including ribbed, twisted, wire coil, vane turbulators, spherical turbulators, etc. Each type has advantages and disadvantages regarding heat transfer enhancement and pressure drop. Gill *et al.,* [7] carried out an experiment in which they explored the effect of the position of the gap in the arc rib on the Nu and the friction factor. Placing a gap in a continuous arc rib enhanced the 'Nu' and 'f' due to flow mixing. The THPP of broken arc rib roughened duct outperforms that of continuous arc rib. Dezan *et al.,* [8] performed a parametric sensitivity analysis of an SAH vortex generator for Re of 5,000 to 10,000. The channel's performance is evaluated by varying nine input parameters linked to the delta winglet pairs. Manjunath *et al.,* [9] studied the impact of spherical turbulence generators on the SAH. According to the findings, the roughness pitch and size of the spherical turbulator have a considerable impact on the THPP of the SAH.

Kumar *et al.,* [10] carried out an experiment and studied the effect of sun intensity on the thermal performance of a herringbone corrugated finned SAH. Kottayat *et al.,* [11] conducted exergy research to assess the impact of secondary flow produced by V-ribs on the overall performance of a triangular SAH. Zhao *et al.,* [12] investigated the convective heat transfer augmentation and friction loss behaviours for turbulent flow using arrays of variably shaped ribs combined with delta winglet vortex generator pairs on the absorber plate of a SAH. Amit *et al.,* [13] suggested a revolutionary design of counter-flow curved double-pass SAH with increased turbulence, longer duct length, and fewer top losses, yielding nearly double the efficiency of a standard collector. According to the experimental results of Skullong *et al.,* [14], the combined rib and groove on the absorber duct give a higher value of Nu and friction factor. According to Mahanand *et al.,* [15], the Nu for SAH with inverted-T ribs is better for the examined Reynolds number range. According to Mahanand *et al.,* [16], the turbulators with the highest heat transfer and the least pressure drop in the studied parametric range may be considered a sustainable design. Doan Thi *et al.,* [17] reviewed and analyzed three mathematical models for predicting air collector temperature drawn from 30 publications between 1980 and 2022. The models are based on heat exchanger surfaces and airflow. The study finds that the temperatures of the air exiting the collector are similar, with the highest deviation occurring at 8 AM. Model 3, corresponding to transient conditions, is recommended for models with negligible plate and glass cover thickness.

A numerical simulation of a solar air heater with a transverse equilateral triangular ribbed surface was conducted by Yadav *et al.,* [18], utilizing ANSYS FLUENT 12.1 for thermal and flow properties, and an optimum thermal enhancement factor of 1.99 was obtained. The same authors investigated the impact of artificial roughness on heat transfer in solar air heater ducting. It numerically analyzes an absorber plate with rib roughness, revealing that adding ribs can enhance system performance. The study investigated turbulent airflow for various rib arrangements and developed a new heat transfer correlation for rib-roughened solar air heaters [19]. Susama *et al.,* [20] investigated the convective heat transfer and friction factor of turbulent airflow in a channel air heater with isosceles triangular grooves combined with transverse baffles. Experiments were conducted in a rectangular channel with different groove depths, inclination angles, and triangular directions. Results showed that isosceles triangular grooves significantly impacted heat transfer rate and friction factor compared to smooth-wall channels. Combining grooves with transverse baffles provided higher heat

transfer rates and friction factors. The maximum thermal performance enhancement was achieved with 30° down-stream grooves. Neural network models were designed to predict the thermal enhancement factor. Kumar *et al.,* [21] examined a solar air channel's heat transfer and friction characteristics with a discretized broken V-pattern baffle on a heated plate. The study investigates the impact of geometrical parameters on the channel's performance, particularly gap width and location. The optimal values of roughness parameters enhanced the channel's performance by 4.47 times compared to the channel without it. The thermal-hydraulic performance parameter had the highest value at 3.14.

Numerous studies have been undertaken using various approaches for heat transfer improvement of a flat plate air heater, as evidenced by the literature studies. It is also clear that varied configurations result in improved air heater performance factors and an incremental trend in frictional factors. As a result, the best turbulator design is being considered, which is predicted to result in improved heat transfer enhancement with minimal frictional loss. Using turbulators invariably increases the pressure drop across the flow, which must be limited to ensure that a given design of turbulators effectively enhances heat transfer without imposing a considerable pressure drop penalty across the flow. In this regard, extensive numerical and experimental analyses have proposed many design configurations of turbulators that could provide enhanced heat transfer with lower pressure drop penalties. However, every design has been found to have a range of flow Reynolds numbers beyond which the rise in pressure drop overshoots the corresponding gain in heat transfer, thereby making the turbulator design useless. Hence, this study is motivated to develop better designs to improve the thermo-hydraulic performance for a wide range of flow Reynolds numbers.

Chamfered turbulators are commonly used in various heat exchangers and cooling systems. The primary goal is to increase the convective heat transfer coefficient between the fluid and the surface. These turbulators are essentially small, angled protrusions or dimples placed on the inner surface of a tube or duct through which a fluid flows. The chamfered shape refers to the angled or bevelled edges of these turbulators. They are designed to disrupt the flow of the fluid, creating turbulence and improving heat transfer in several ways. In this study, the effective thermal performance of a flat plate solar air heater with a circular chamfered turbulator (CCT) design is numerically evaluated for different flow attack angles and sizes. Turbulators are attached to facing both upstream and downstream of the flow. The chamfered design often involves introducing inclined surfaces (chamfers) to disrupt the fluid flow and promote turbulence. Computational fluid dynamics (CFD) software simulated the fluid flow and heat transfer characteristics of chamfered turbulator design. This helps to evaluate different geometries and optimize the design for maximum heat transfer. Designing chamfered turbulators for heat transfer involves creating structures within a fluid flow system to enhance heat transfer between the fluid and a solid surface.

Thus, based on the extensive literature review, the following hypothesis is framed for the current work. Research Hypothesis: Develop a novel turbulator design that can enhance thermo-hydraulic performance across a wide range of mass flow rates.

2. Methodology

2.1 Base and Chamfered Model of SAH

A detailed parametric study is carried out using the numerical tool to get the optimized design of the turbulator. The numerical analysis includes geometric modelling, mesh generation, grid-independent tests, and invoking the boundary conditions. After convergence of the solution is achieved, the results are captured, and the flow physics is analyzed using contour and streamline

plots. The basic geometrical configuration of the SAH used in the present analysis is shown in Figure 1. The SAH consists of three sections, namely the inlet duct, absorber duct, and outlet duct. A 1 mm thickened absorber plate is attached above the absorber duct. The numerical results for the base model were validated, with the experimental results carried out with solar simulators and necessary controlling and measuring equipment [20].

The copper-chamfered cylindrical turbulators are installed beneath the absorber plate, as shown in Figure 2a. In these two cases, one is modelled such that the chamfered angle faces toward the flow, as shown in Figure 3, and another one is modelled such that the chamfered angle faces opposite to the flow direction, as depicted in Figure 4. The turbulators' core diameter (d) ranges from 3 mm to 7 mm. For each configuration, there are three rows of turbulators with equal spacing. 200mm is the pitch distance between two consecutive rows of turbulators. The flow attack angles of the chamfered turbulator are 30°, 45° and 60°, respectively. The physical characteristics of the chamfered turbulator are depicted in Figure 2b. The parameters considered for the study are depicted in Table 1.

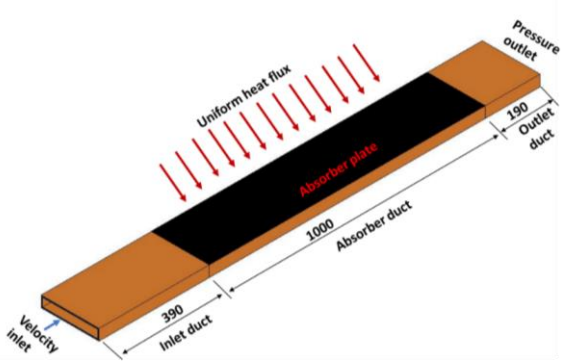

Fig. 1. Basic geometry of the solar air heater [11]

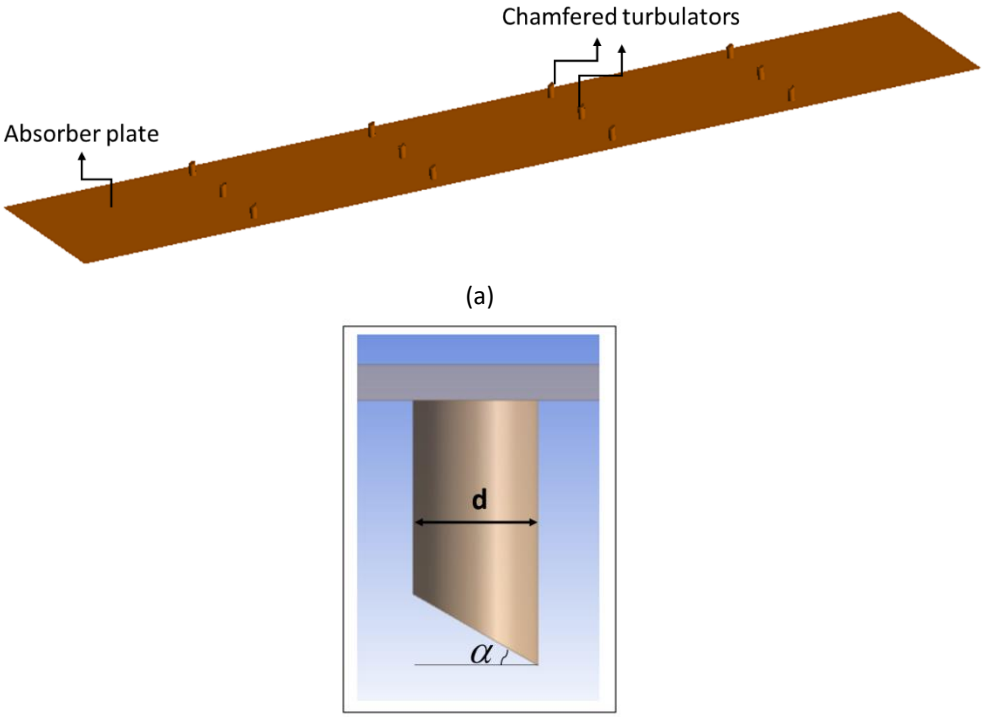

Fig. 2. a) SAH absorber plate with chamfered turbulators b) Physical characteristics of chamfered turbulator

Table 1
Parametric study of the chamfered turbulators

Flow direction	Diameter, d (mm)	Chamfered angle, α (°)		
Upstream	3	30	45	60
	5	30	45	60
	7	30	45	60
Downstream	3	30	45	60
	5	30	45	60
	7	30	45	60

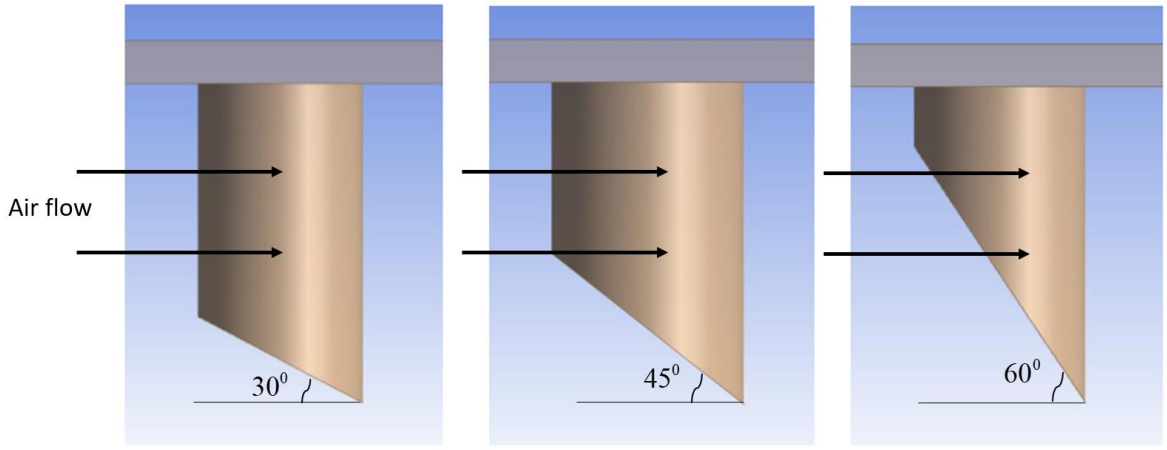

Fig. 3. Chamfered toward the downstream side of the flow

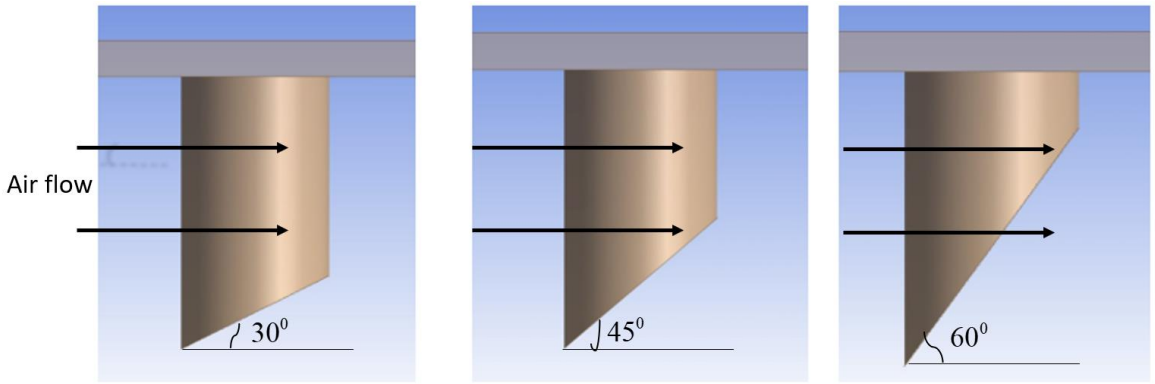

Fig. 4. Chamfered toward the upstream side of the flow

2.2 Mesh Generation

Figure 5 depicts a localized view of the meshed domain, with the chopped part highlighted to represent the finer mesh near the wall. Figure 6 represents the grid-independent test.

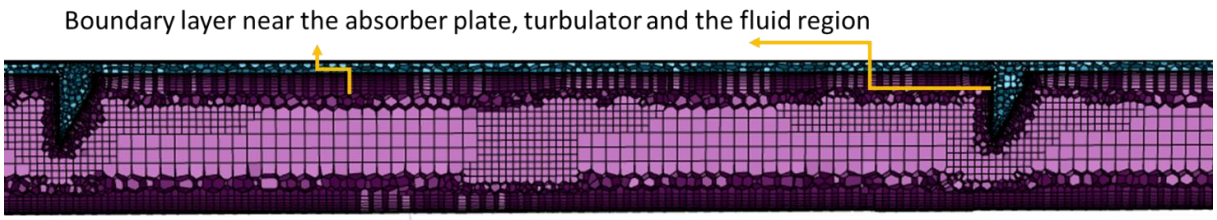

Fig. 5. Meshed air duct portion (Close-up view near the plate and fluid interface region)

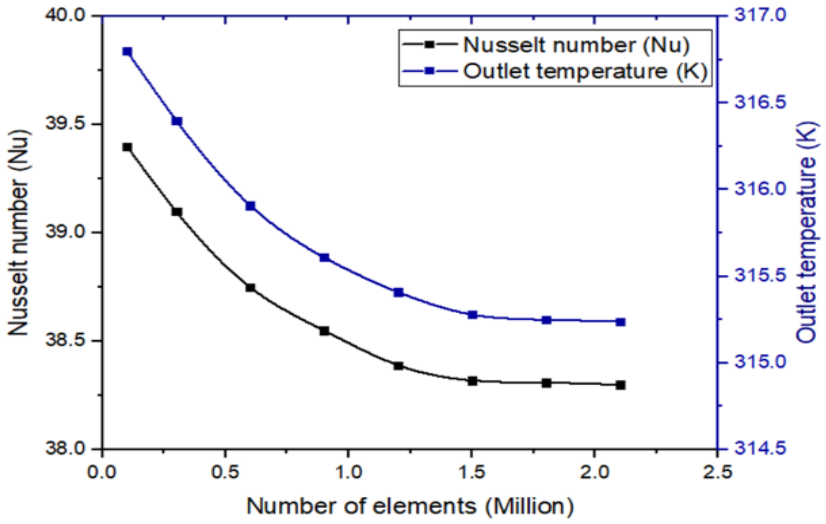

Fig. 6. Nu and outlet temperature variation for the control volumes

2.3 Governing Equation and Performance Parameters

Governing equations are partial derivative equations based on mass, momentum, and energy conservation, given in Eq. (1) to Eq. (10). The performance parameters are represented in Eq. (11) to Eq. (14).

$$\frac{\partial \bar{u}}{\partial x}+\frac{\partial \bar{v}}{\partial y}+\frac{\partial \bar{w}}{\partial z}=0 \tag{1}$$

$$\frac{\partial}{\partial x_i}\left(\rho \bar{u}_i \bar{u}\right)=-\frac{\partial \bar{p}}{\partial x_i}+\frac{\partial}{\partial x_i}\left(\mu\left(\frac{\partial \bar{u}_i}{\partial x_j}+\frac{\partial \bar{u}_j}{\partial x_i}-\frac{2}{3}\delta_{ij}\frac{\partial \bar{u}_l}{\partial x_l}\right)\right)-B_i-\frac{\partial}{\partial x_i}\left(\overline{\rho u_i' u_j'}\right) \tag{2}$$

$$-\rho\left(\overline{u_i' u_j'}\right)=\mu_t\left(\frac{\partial u_i}{\partial x_j}+\frac{\partial u_j}{\partial x_i}\right)-\frac{2}{3}\left(\rho k+\mu_t\frac{\partial u_k}{\partial x_k}\right)\delta_{ij} \tag{3}$$

$$\frac{\partial}{\partial t}(\rho k)+\frac{\partial}{\partial x_i}(\rho k u_i)=\frac{\partial}{\partial x_j}\left(\Gamma_k\frac{\partial k}{\partial x_j}\right)+G_k-Y_k \tag{4}$$

$$\frac{\partial}{\partial t}(\rho \omega)+\frac{\partial}{\partial x_j}\left(\rho \omega u_j\right)=\frac{\partial}{\partial x_j}\left(\Gamma_\omega\frac{\partial \omega}{\partial x_j}\right)+G_\omega-Y_\omega+D_\omega \tag{5}$$

$$\frac{\partial(\rho k)}{\partial t}+\frac{\partial(\rho k u_i)}{\partial x_i}=\frac{\partial}{\partial x_j}\left(\frac{\mu_i}{\sigma}\frac{\partial k}{\partial x_j}\right)+2\mu_i E_{ij}E_{ji}-\rho\varepsilon \tag{6}$$

$$\frac{\partial(\rho\varepsilon)}{\partial t}+\frac{\partial(\rho\varepsilon u_i)}{\partial x_i}=\frac{\partial}{\partial x_j}\left(\frac{\mu_t}{\sigma_\varepsilon}\frac{\partial \varepsilon}{\partial x_j}\right)+C_{1\varepsilon}\frac{\varepsilon}{k}2\mu_t E_{ij}E_{ji}-C_{2\varepsilon}\rho\frac{\varepsilon^2}{k} \tag{7}$$

$C_\mu=0.09;\sigma_k=1.00;\sigma_\varepsilon=1.30;C_{1\varepsilon}=1.44;C_{2\varepsilon}=1.92$

'k' is the Turbulence kinetic energy, and '***ε***' is the turbulence-specific dissipation rate.

$$\frac{\partial}{\partial x_i}(\rho E u_i)=-\frac{\partial}{\partial x_i}(p u_i)+\frac{\partial}{\partial x_i}\left(k_{eff}\frac{\partial T}{\partial x_i}\right) \tag{8}$$

Where $E=h_e-\frac{p}{\rho}+\frac{V^2}{2}$ (9)

$$\rho\frac{\partial h_e}{\partial t}=k\left(\frac{\partial^2 T}{\partial n^2}\right)+S_h \tag{10}$$

Nusselt number, $Nu=\frac{hD_h}{k}$ (11)

Friction factor, $f=\frac{(\Delta p)D_h}{2\rho L V_m^2}$ (12)

Thermo Hydraulic Enhancement factor, $THEF=\frac{\left(\frac{Nu}{Nu_s}\right)^{1/2}}{\left(\frac{f}{f_s}\right)^{1/3}}$ (13)

Absorber plate temperature coefficient, $C_{ta}=\frac{(T_p-T_i)}{T_i}$ (14)

2.4 Boundary Conditions

Various boundary conditions used for the current CFD analysis are listed in Table 2. The mass flow rate is computed in terms of the Re. In the experimental investigation, the prescribed heat flux is applied to the absorber plate under the intensity of solar radiation. Air is the working fluid and is a function of temperature. Air properties are defined in terms of temperature and given by Eq. (15), Eq. (16) and Eq. (17) as per the work performed by W. Gao *et al.,* [21].

$$\rho = 3.9147 - 0.016082T + 2.9013\times10^{-5}T^2 - 1.9407\times10^{-8}T^3 \quad (15)$$

$$\mu = \left(1.6157 + 0.06523T - 3.0297\times10^{-5}T^2\right)\times10^{-6} \quad (16)$$

$$k = \left(0.0015215 + 0.097459T - 3.3322\times10^{-5}T^2\right)\times10^{-3} \quad (17)$$

The authors in their previous research [20] conducted a turbulence model suitability test and found that RNG k-epsilon model is the suitable turbulence model. Accordingly, the present numerical work also incorporated the RNG k-epsilon model to simulate the turbulence.

Table 2
Boundary conditions adopted in the study

Boundary	**Conditions applied**
Inlet	Mass flow inlet (As per Reynolds number); Temperature (Ambient condition)
Outlet	Pressure outlet (Ambient condition)
Absorber plate	Heat flux (W/m^2)
Wall	No slip (Wall of the absorber duct, inlet, and outlet)
Air property	Polynomial equations (For density, viscosity, and thermal conductivity) are given in Eq. (15), Eq. (16) and Eq. (17).
Region	Absorber plate (Solid); Air inside the duct (Fluid)

2.5 Validation Studies

Before starting the CFD work, validating the CFD model with established experimental results available in the literature for the baseline model of solar air heaters (without turbulators) is necessary. The authors have experimented on the SAH base model [20]. As a secondary check, the Dittus Boelter equation, as depicted in Eq. (18), a well-known correlation to predict the Nusselt number, is also verified for the analysis.

$$Nu = 0.023\,\mathrm{Re}^{0.8}\,\mathrm{Pr}^{0.4} \quad (18)$$

Figure 7 shows the variation of Nu with respect to Re. It is found that the error margin between the experimental and CFD work exists below 5%, whereas the error margin is within 3% when compared to the CFD results with correlation.

Similarly, the pumping power is plotted against Re for the experimental and CFD analyses. It is shown in Figure 8. It is found that CFD results and the experimental results vary within the range of ± 10%.

The negligible nonconformities seen in these values are due to the truncational and rounding-off errors. As a result, the CFD model employed in the investigation is obviously in decent concurrence with the experimental results. Hence, the CFD model is presumed reliable in envisaging reasonably acceptable results in terms of Nusselt number and pumping power requirements.

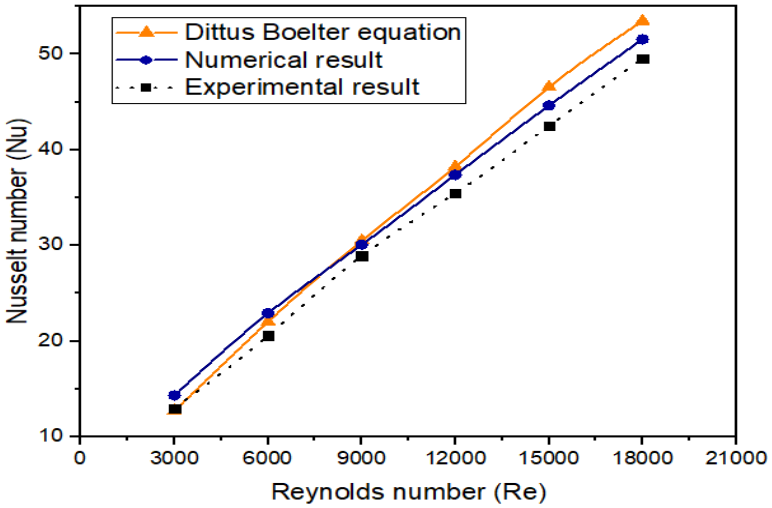

Fig. 7. Validation of the numerical studies for Nusselt number

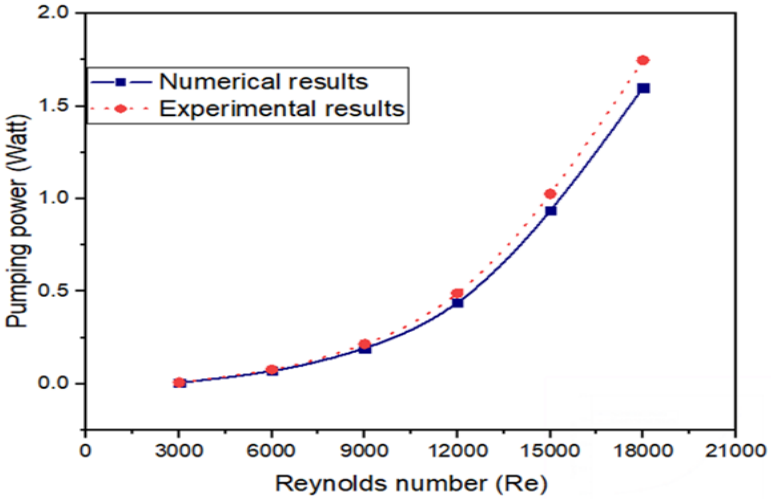

Fig. 8. Validation of the numerical studies for pumping power

3. Results and Discussion

This section initially explains the effect of circular chamfered turbulators on flow physics. This is followed by the discussion on the effect of placement of the turbulators with fixed diameters having variable chamfered angles and vice versa. Finally, the effect of the optimized chamfer facing with respect to the flow direction is discussed.

3.1 Effect of Chamfered Turbulators on Flow Physics

Chamfered turbulators enhance heat transfer and fluid mixing by introducing turbulence into the flow. The impact on flow physics includes improved heat transfer, increased turbulence, higher pressure drop, potential flow stability issues, and the ability to control and manipulate flow patterns. The effectiveness of chamfered turbulators in improving heat transfer and mixing depends on several factors, including their geometry, spacing, and the properties of the fluid. Optimizing the design of turbulators often involves a trade-off between improved heat transfer and increased pressure drop. The SAH model is sliced in the x, y, and z directions (isosurfaces) to analyze the flow structure. The x-

plane represents the flow direction, the y-plane represents the height of the duct, and the z-plane indicates the width of the duct.

Figure 9 shows the velocity variation along the flow direction and width. When the flow strikes the turbulators, it forms the recirculation zone. Hence, velocity variations near the turbulators can be seen in the contour plot.

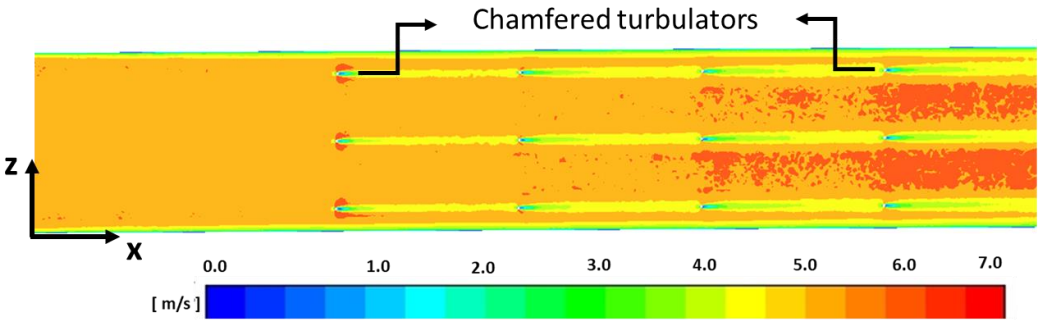

Fig. 9. Bottom view of the velocity contour plot in the z-x plane

Figure 10 represents the temperature variation along the flow direction with respect to the width of the duct. Air enters the inlet duct with ambient temperature. As the flow passes through the duct, it absorbs the heat from the absorber plate and gradually gets heated. Near the Circular Chamfered Turbulators, hot zones indicate the heat carried by the turbulators towards the depth of the duct. Figure 11 shows the temperature gradient along the depth of the SAH. Heat transfer from the top plate to the centre of the duct can be seen in the contour plot.

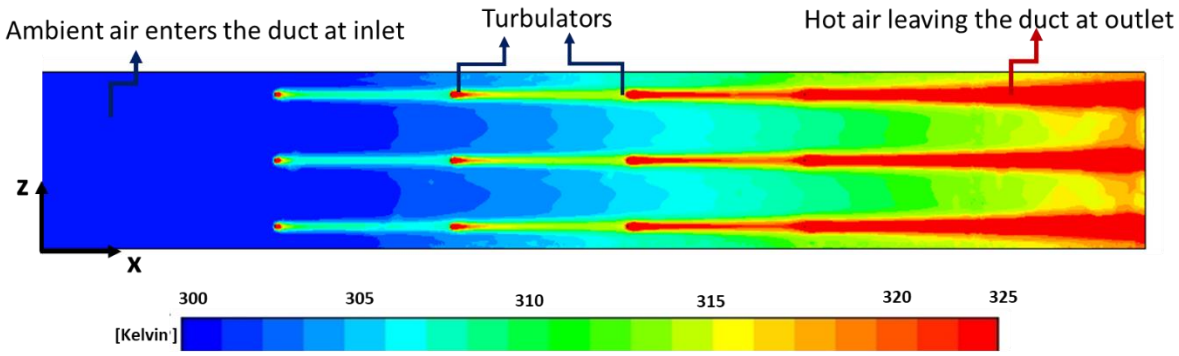

Fig. 10. Bottom view of the temperature contour plot in the z-x plane

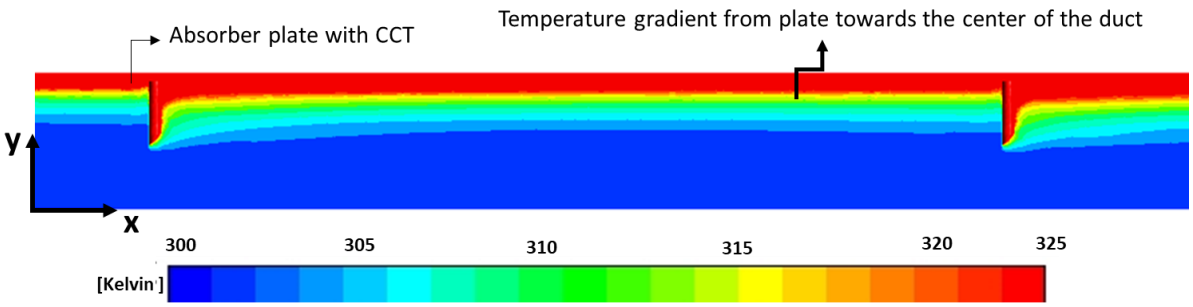

Fig. 11. Side view of the temperature contour plot in the x-y plane

Figure 12 shows the pressure contour plot along the flow direction. When the flow strikes the turbulators, a higher pressure drop is observed. At the same instant, the opposite side of the turbulators experiences a lower pressure drop.

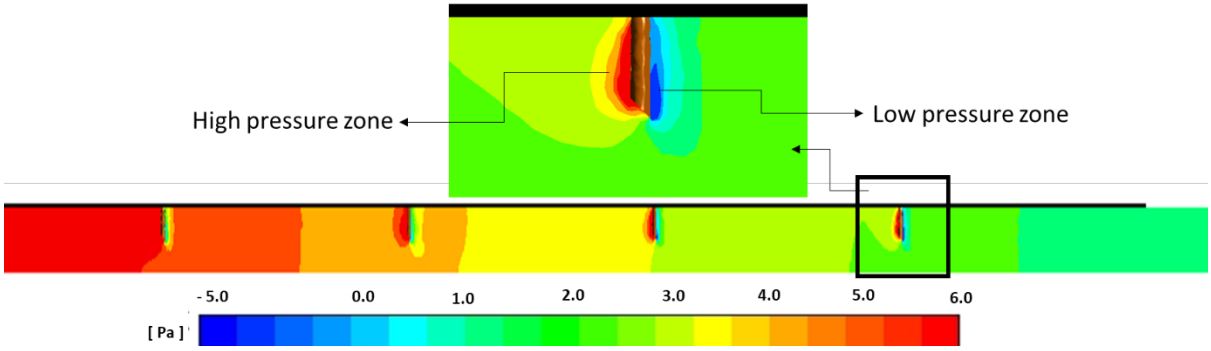

Fig. 12. Side view of the pressure contour plot in the x-y plane

Figure 13 indicates the velocity streamlines near the circular chamfered turbulators. Due to the obstruction in the flow, the flow recirculation can be seen. Near the chamfered face, along with flow recirculation eddies, a large wake formation can also be seen in Figure 14. Smaller eddies and recirculation promote heat transfer, whereas larger eddies adversely affect the heat transfer rate.

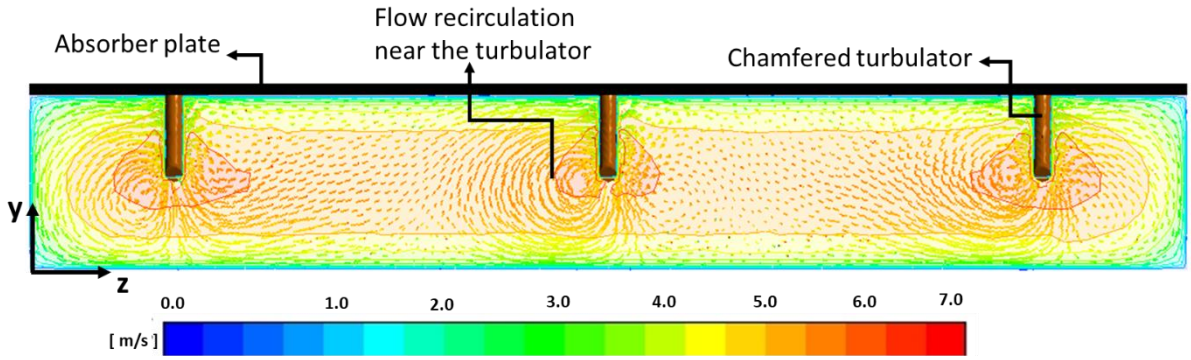

Fig. 13. Velocity streamlines near the CCT in the y-z plane

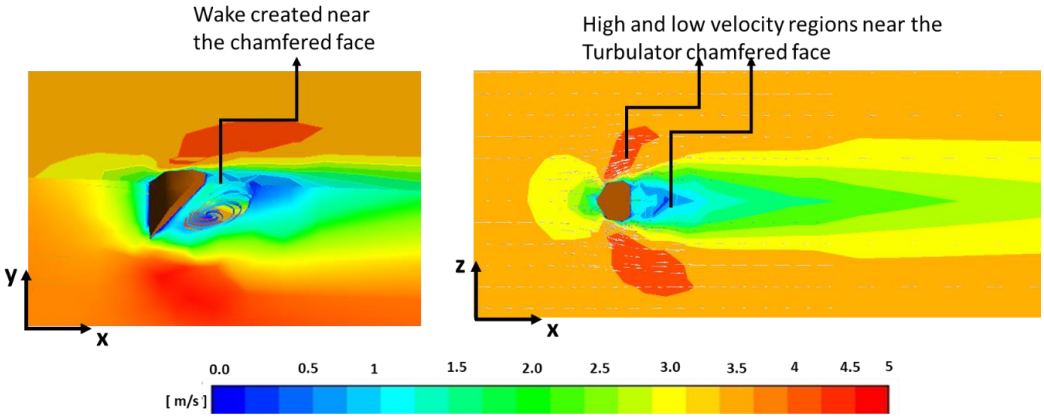

Fig. 14. Wake created near the Chamfered face indicated in (a) y-x plane, (b) z-x plane

3.2 Effect of the Turbulator Diameter and Chamfered Angle – Downstream Arrangement

Circular chamfered turbulator angles vary from 30° to 60° in steps of 15° for a particular turbulator diameter. The turbulators are arranged in the downstream arrangement.

Figure 15a represents the Nu versus Re plot for the turbulator diameter of 3 mm, with different chamfered angles studied. It is observed that for all the cases, Nu increases with Re for all the flow ranges and all the configurations tested. A chamfered angle of 30° shows the highest values of Nu for all the Reynolds numbers tested. As the chamfered angle increases, the heat transfer rate decreases are observed. A chamfered angle of 60° shows the lowest value of the Nu throughout the flow Reynolds number.

Figures 15b and 15c represent the Nu versus Re plot for the turbulator diameter of 5 mm and 7 mm with the different chamfered angles studied. A continuous increase in the Nu with Re is observed for both cases. The chamfered angle of 30° shows the highest values of Nu, followed by 45° and 60° chamfered angles. As the chamfer angle increases, a larger recirculation region forms, adversely affecting heat transfer. Therefore, lower values for Nu are noticed for the highest chamfer angle of 60°.

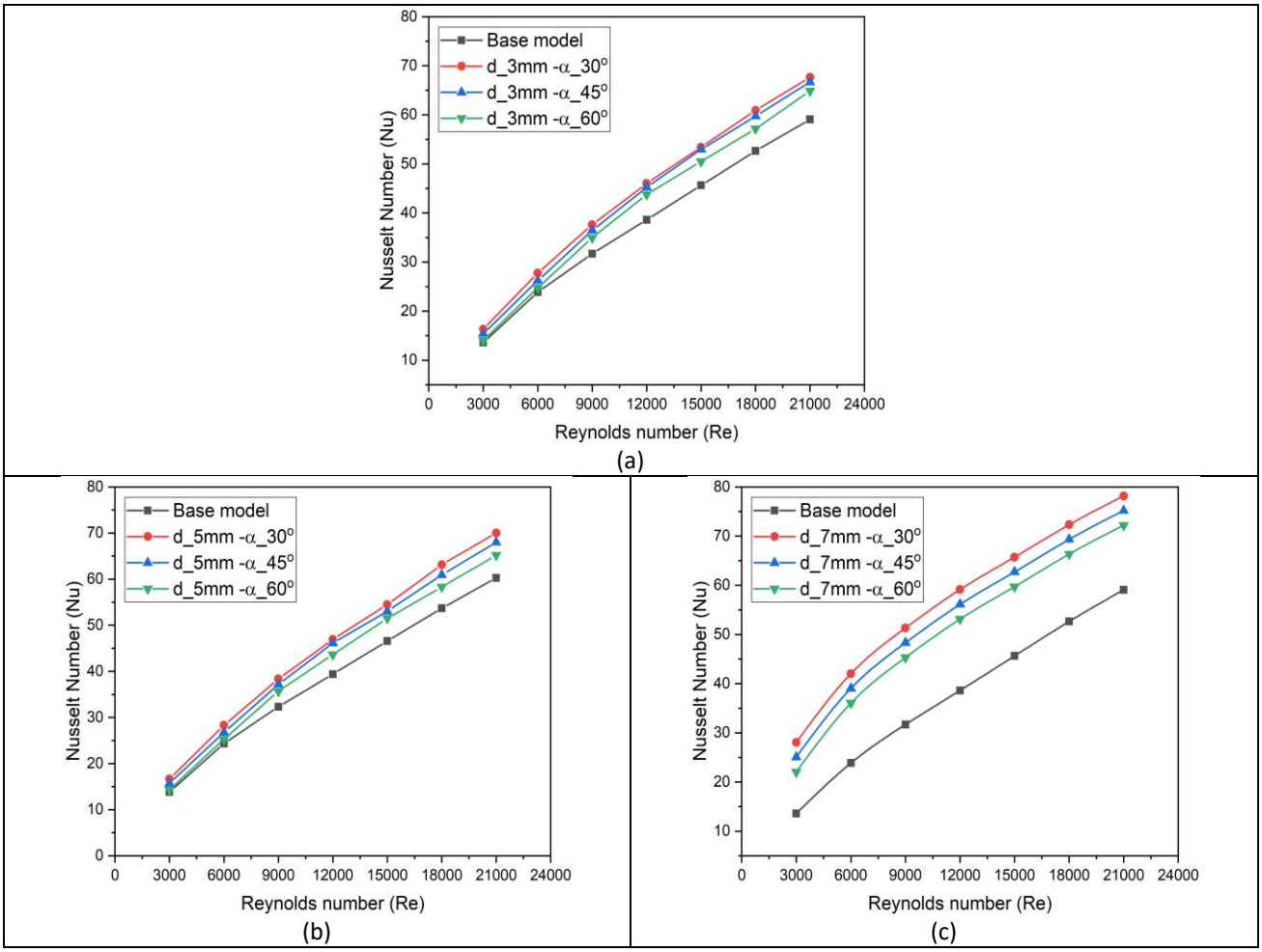

Fig. 15. Variation of Nu versus Re with different chamfered angles for the turbulator diameter of (a) 3 mm, (b) 5 mm, (c)7 mm

Figure 16 shows the variation Nu for the different diameters of turbulators tested with a chamfer angle of 30°. As the diameter of the turbulators increases, the area exposed to the heat transfer also

increases; hence, higher values of the Nu are observed for the larger diameter of the turbulators. The highest value of the Nu is obtained for the turbulator diameter of 7 mm and chamfer angle of 30°, and the lowest values are observed for the least diameter of 3mm turbulator configuration. With somewhat more flow disturbance, the air stream passes beneath the turbulator. Nonetheless, with a flow attack angle of 30° at a diameter of 7 mm, stronger and larger longitudinal vortices emerge as the diameter of chamfered turbulators increases due to increased flow interference. It is observed that a 3 mm diameter produces sufficient turbulence to increase the flow's Nu without significantly disrupting it. Counter-rotating vortices are produced by chamfered turbulators, which increase turbulence and push air around the flat plate turbulator. This significantly improves the heat transfer. Downstream of the flat plate, the chamfered turbulator design improves the turbulent flow. The chamfered turbulator is added to increase heat transfer. This creates vortices that aid in the airflow in the plate core as it approaches the absorber plate's surface. The airflow impingement on the side of the chamfered turbulator that is directly upstream is likewise found to diminish when the flow attack angle increases. This is because the chamfered turbulators provide less obstruction. This reduces heat transfer on the upstream side of the chamfered turbulator.

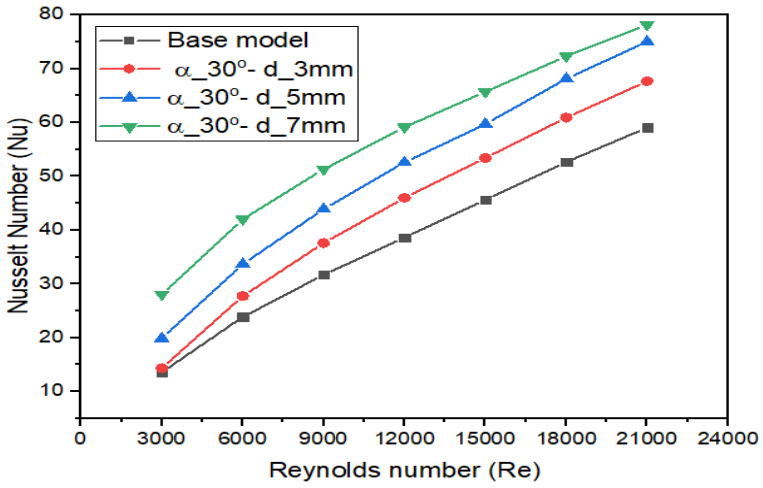

Fig. 16. Nusselt number versus Reynolds number for the chamfered angle of 30° with diameters of 3mm, 5mm, and 7mm

Because of the impingement brought on by the obstructive chamfered turbulator, it is seen that there is a greater increase in the Nusselt number at the upstream region of the plate. As a result, by impinging the airflow on the next turbulator, the chamfered turbulator can completely bend it, increasing the heat transfer rate. In contrast, there are no obstacles in the space between two successive turbulators. As a result, the chamfered turbulator has little effect on the path lines. In the vicinity of the chamfered turbulator, the Nusselt number has gone up. This suggests that heat transport is more significant in this area.

Absorber plate temperature data depicted the amount of heat transferred from the absorber plate to the air passing through the plate. The absorber plate temperature coefficient is defined as the ratio of absorber plate temperature and inlet temperature difference to the inlet temperature of the air. Figure 17 shows the absorber plate temperature coefficient versus Re for the different diameter turbulators tested with the chamfer angle of 30°. The lowest temperature is noticed for the 7 mm diameter turbulators due to their higher exposure area to the airflow. The base model average plate temperature coefficient is higher than all the configurations tested due to inefficient heat transfer from the surface of the absorber plate.

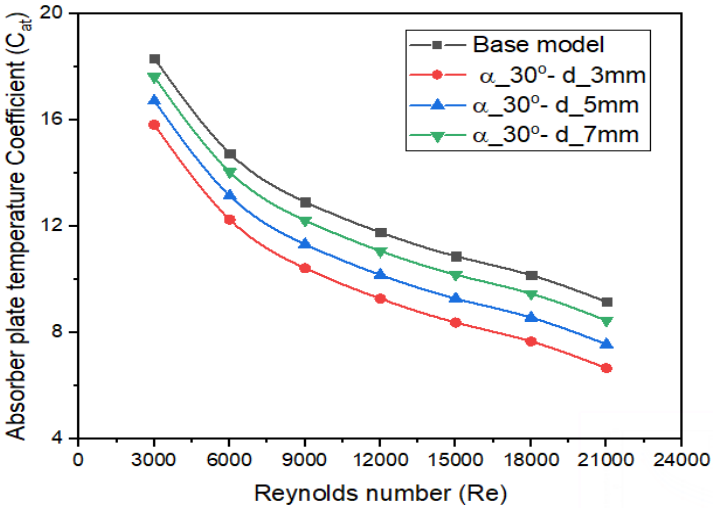

Fig. 17. Absorber plate temperature coefficient versus Re for the different diameter turbulators tested with the chamfer angle 30°

As the air moves through the absorber duct, it absorbs the solar radiation and gets heated. Figure 18 represents the increment in the air temperature for the various configurations tested. The highest temperature is noticed for the highest turbulator diameter of 7 mm and the lowest chamfered angle of 30°. As the tabulator's diameter decreases and the chamfer angle increases, the heat transfer rate decreases; hence, lower outlet temperature values were noticed in these cases.

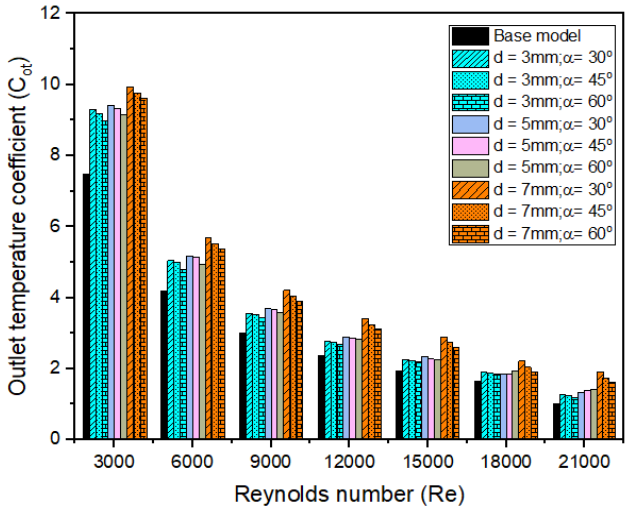

Fig. 18. Outlet temperature coefficient for the various configurations studied

Chamfered turbulators, when introduced into a fluid flow, can significantly alter the velocity streamlines. The effect on streamlines depends on the design and placement of the turbulators, as well as the characteristics of the fluid and the flow regime. Chamfered turbulators can lead to vortices and swirls forming in the flow. These vortices can create complex and intricate velocity streamlines. Figure 19 represents the flow streamline plots over the 30°, 45° and 60° chamfered circular turbulators. Flow initially hits the tabulator's front face and deviates toward the upstream side. Large wake regions are noticed in this process as the turbulator chamfered angle increases. A circular chamfered angle of 60° shows the large void formation at the backside of the CCT.

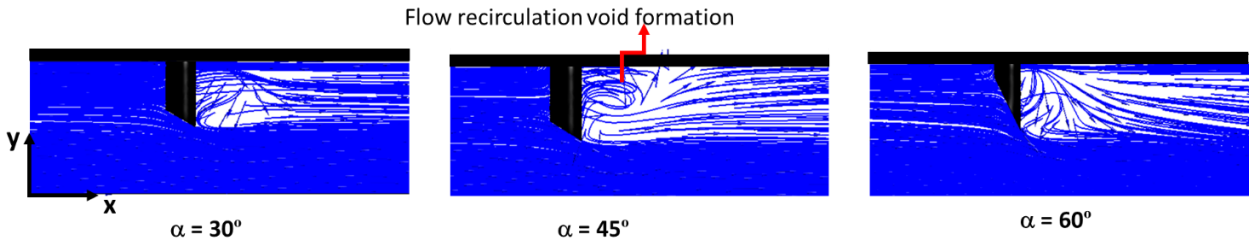

Fig. 19. Velocity streamlines near the different angle chamfered turbulators

Figure 20, Figure 21, and Figure 22 represent the variation of the velocity pressure and temperature when the flow passes through the 30°, 45°, and 60° chamfered circular turbulators. The introduction of chamfered turbulators can have an impact on the stability of the flow. Depending on the geometry and arrangement of the turbulators, there may be an increased risk of flow separation or other flow instabilities. Proper design and placement are essential to minimize adverse effects on flow stability. Comparatively, the low-velocity region and the higher-pressure drop are noticed for the 60° chamfered turbulators. As the fluid encounters the chamfered edges, it is deflected and forced to follow a different path. Chamfered turbulators can introduce pressure gradients in the flow field, affecting the velocity distribution. The pressure gradients can change the velocity streamlines as the fluid is pushed or pulled in different directions.

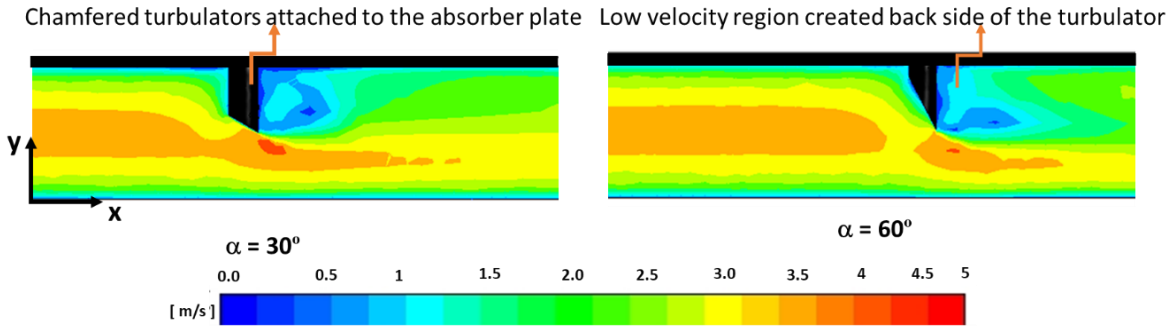

Fig. 20. Velocity contour plots at chamfered angle of 30° and 60°

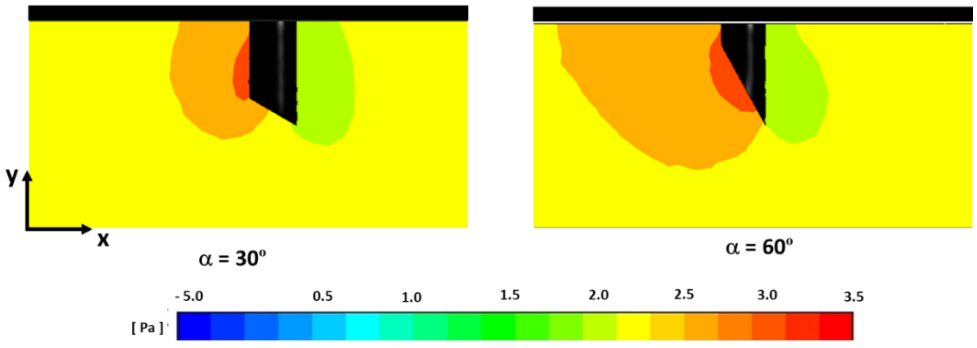

Fig. 21. Pressure contour plots at chamfered angle of 30° and 60°

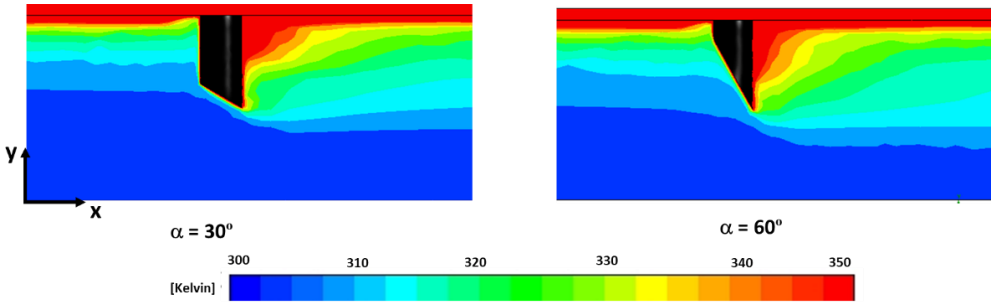

Fig. 22. Temperature contour plots at chamfered angle of 30° and 60°

From the design point of view, for the downstream arrangement of chamfered turbulators, it is found that the chamfer angle of 30° is found to be the optimum chamfer angle for the turbulator in a solar air heater for the range of flow Re chosen for the study.

3.3 Effect of the Turbulator Diameter and Chamfered Angle – Upstream Arrangement

When chamfered turbulators are placed in an upstream-facing orientation, they are positioned so that the chamfered edge faces the incoming fluid flow. This orientation effectively generates turbulence and disrupts the boundary layer near the leading edge of the turbulator. As the fluid flows over the chamfered surface, it experiences a sudden change in flow direction, which enhances mixing and heat transfer. Therefore, upstream-facing turbulators increase heat transfer rate significantly with higher pressure drop.

Downstream-facing turbulators are oriented such that the chamfered edge faces the flow direction. Geometry is modelled by making the chamfered turbulators face the flow's downstream side, and analysis is carried out. Figure 23 shows the Nu variation with the Re for all the downstream-facing turbulator configurations. A higher-diameter turbulator with a lower chamfer angle performs better than all the configurations. Chamfer angle of 30° and turbulator diameter of 7 mm give the highest value of the Nu in the configurations tested. Nu variation trends are similar to the upstream-facing turbulators with slightly lesser values.

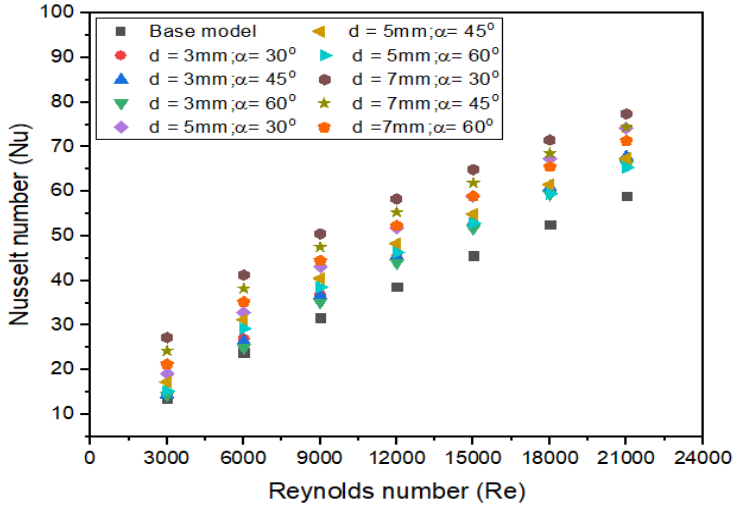

Fig. 23. Nu versus Re plots all configurations tested at various turbulator diameters and angles when the chamfer faces the upstream side

Upstream-facing turbulators create large void regions near the chamfered faces that decrease the heat transfer rate, and hence, lower values of Nu are observed. Chamfered turbulators are primarily employed to enhance convective heat transfer. The chamfered edges create turbulence in the flow, which increases the heat transfer coefficient between the fluid and the solid surface. While downstream turbulators still disrupt the boundary layer, their impact on heat transfer is generally less pronounced than upstream-facing turbulators. Downstream-facing turbulators are often used when the primary goal is to control flow separation or reduce pressure drop rather than maximizing heat transfer.

3.4 Effect on the Pumping Power Requirement

Figure 24 illustrates the pressure drop variation across different configurations tested with an optimum 30° chamfered angle for various chamfered turbulator diameters. An increase in the diameter of chamfered turbulators corresponds to an increase in fluid path restriction, resulting in a higher pressure drop and an elevated demand for pumping power. With an accelerated flow velocity, there is a concurrent rise in pressure. Notably, the chamfered turbulator with a diameter of 7mm exhibits the highest pumping power requirement, followed by those with diameters of 5mm and 3mm.

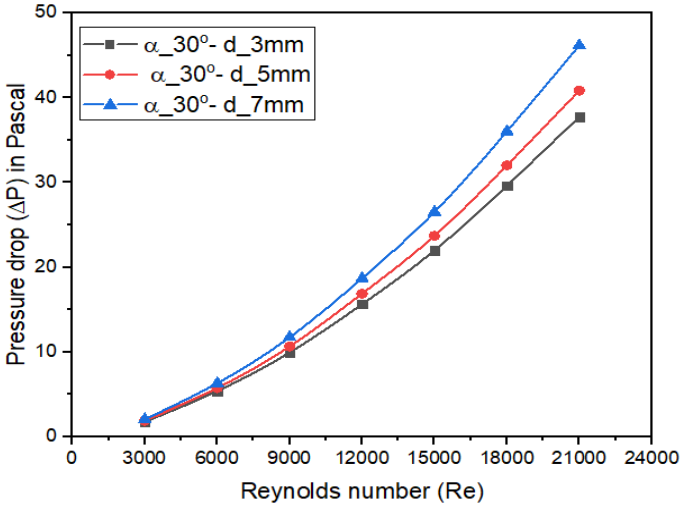

Fig. 24. Pressure drop plots for optimized chamfer angles and various diameter values

3.5 Effect on the Thermohydraulic Enhancement Factor (THEF)

Figure 25 illustrates the THEF variation with the Reynolds number for chamfered turbulators with an optimum 30° chamfered angle and a diameter of 7mm. As the Reynolds number increases, there is a corresponding rise in pumping power requirements, leading to a decrease in THEF improvement. Among the tested diameters, the 7mm diameter turbulator exhibits the highest THEF of 1.15 at a Reynolds number of 3000. Up to a Reynolds number of 15000, the 7mm diameter chamfered turbulator demonstrates enhanced heat transfer with a negligible pressure drop penalty.

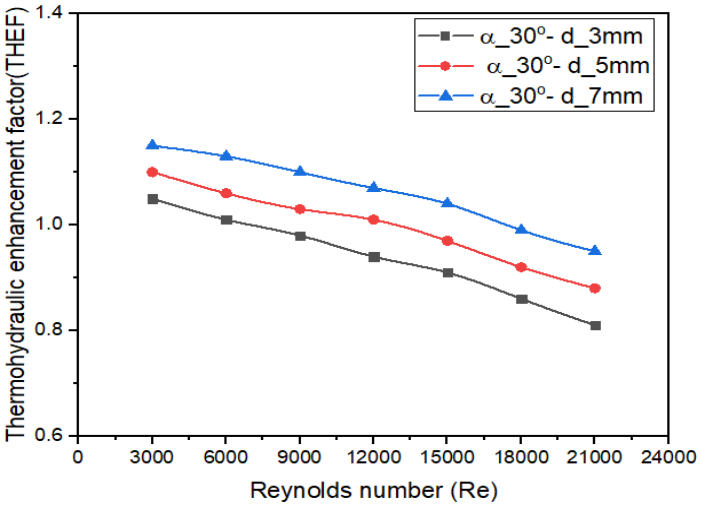

Fig. 25. Pressure drop plots for optimized chamfer angles and various diameter values

However, beyond a Reynolds number of 15000, the pressure drop becomes more prominent than the gain in heat transfer, resulting in a negative net improvement. Consequently, for Reynolds numbers exceeding 15000, THEF values fall below unity, as depicted in Figure 25. A similar trend is observed for 5mm and 3mm diameters, where a decrease in the THEF becomes noticeable beyond Reynolds numbers of 12000 and 6000, respectively.

4. Conclusions

Chamfered turbulators in the flow path disrupt the laminar flow and promote turbulence generation. This increased turbulence aids in mixing the fluid.

i. The efficiency is primarily affected by an increase in effective area and the chamfer angle of the turbulator inserts.
ii. For inclination angles against the flow of air (downstream), better Nu values were obtained compared to inclination angles towards the flow of air (upstream).
iii. The chamfer angle of 30° a diameter of 7 mm placed against the flow of air gave the best Nu value throughout the analysis.
iv. TEF is found to increase with the increasing diameter of the turbulator, whereas it decreases with increasing chamfer angle.
v. For a given chamfered turbulator, α = 30° placed against the flow of air at a diameter of 7 mm yielded a considerably more significant thermal enhancement factor of 1.15 over the spectrum of flow Reynolds number studied.

Acknowledgement

The simulation was carried out at the Department of Mechanical and Industrial Engineering, MIT Manipal, and the authors gratefully acknowledge the computational facilities provided by the institute.

References

[1] Mugisidi, Dan, Berkah Fajar, Syaiful Syaiful, and Tony Utomo. "Solar Still with an Integrated Conical Condenser." *CFD Letters* 15, no. 8 (2023): 122-134. https://doi.org/10.37934/cfdl.15.8.122134.

[2] Boukhriss, Mokhless, Mahdi Timoumi, Adel Jammeli, Mohamed Ali Maatoug, Kamel Zarzoum, Sleh Farhani, and Habib Ben Bacha. "Modeling and Experimental Study of a Water Solar Collector Coupled to Optimized Solar Water Still." *CFD Letters* 15, no. 10 (2023): 23-33. https://doi.org/10.37934/cfdl.15.10.2333.

[3] Del Rio, Jorge Andrés Sierra, Yustin Roman Ardila, Alejandro Ruiz Sánchez, Edwin Correa Quintana, D. Sanin-Villa, C. Arrieta González, and M. Luna-Del Risco. "Numerical Study of the Efficiency of a Solar Panel with Heat Sinks." *CFD Letters* 15, no. 4 (2023): 43-52. https://doi.org/10.37934/cfdl.15.4.4352.

[4] Amrizal, Amrizal. "Effects of Fin Height, Fin Thickness and Reynolds Number on Heat Transfer Enhancement of Flat-Plate Thermal Collector: A Numerical Analysis." *CFD Letters* 15, no. 4 (2023): 53-63. https://doi.org/10.37934/cfdl.15.4.5363.

[5] Azmi, Muhammad Amirul Azwan, Amir Abdul Razak, Muhammad Amir Syahiran Muhammad Tarminzi, Ahmad Fadzil Sharol, Ahmmad Shukrie Md Yudin, and Zafri Azran Abdul Majid. "Hydrodynamics Investigations of Kaffir Lime Leaves Drying in a Swirling Solar Drying Chamber with Inclined Slotted Angle Air Distributor." *CFD Letters* 15, no. 2 (2023): 71-86. https://doi.org/10.37934/cfdl.15.2.7186.

[6] Abdullah, Yussra Malallah, Ghadeer Salim Aziz, and Hussein Kadhim Sharaf. "Simulate the Rheological Behaviour of the Solar Collector by Using Computational Fluid Dynamic Approach." *CFD Letters* 15, no. 9 (2023): 175-182. https://doi.org/10.37934/cfdl.15.9.175182.

[7] Gill, R. S., V. S. Hans, and Sukhmeet Singh. "Investigations on thermo-hydraulic performance of broken arc rib in a rectangular duct of solar air heater." *International Communications in Heat and Mass Transfer* 88 (2017): 20-27. https://doi.org/10.1016/j.icheatmasstransfer.2017.07.024.

[8] Dezan, Daniel J., Andre D. Rocha, and Wallace G. Ferreira. "Parametric sensitivity analysis and optimisation of a solar air heater with multiple rows of longitudinal vortex generators." *Applied energy* 263 (2020): 114556. https://doi.org/10.1016/j.apenergy.2020.114556.

[9] Manjunath, M. S., K. Vasudeva Karanth, and N. Yagnesh Sharma. "Numerical analysis of the influence of spherical turbulence generators on heat transfer enhancement of flat plate solar air heater." *Energy* 121 (2017): 616-630. https://doi.org/10.1016/j.energy.2017.01.032.

[10] Kumar, Rajesh, and Prabha Chand. "Performance enhancement of solar air heater using herringbone corrugated fins." *Energy* 127 (2017): 271-279. https://doi.org/10.1016/j.energy.2017.03.128.

[11] Nidhul, Kottayat, Sachin Kumar, Ajay Kumar Yadav, and S. Anish. "Enhanced thermo-hydraulic performance in a V-ribbed triangular duct solar air heater: CFD and exergy analysis." *Energy* 200 (2020): 117448. https://doi.org/10.1016/j.energy.2020.117448.

[12] Zhao, Zhiqi, Lei Luo, Dandan Qiu, Zhongqi Wang, and Bengt Sundén. "On the solar air heater thermal enhancement and flow topology using differently shaped ribs combined with delta-winglet vortex generators." *Energy* 224 (2021): 119944. https://doi.org/10.1016/j.energy.2021.119944.

[13] Kumar, Amit, Ajeet Pratap Singh, and O. P. Singh. "Performance characteristics of a new curved double-pass counter flow solar air heater." *Energy* 239 (2022): 121886. https://doi.org/10.1016/j.energy.2021.121886.

[14] Skullong, Sompol, Sutapat Kwankaomeng, Chinaruk Thianpong, and Pongjet Promvonge. "Thermal performance of turbulent flow in a solar air heater channel with rib-groove turbulators." *International Communications in Heat and Mass Transfer* 50 (2014): 34-43. https://doi.org/10.1016/j.icheatmasstransfer.2013.11.001.

[15] Mahanand, Yadaba, and Jnana Ranjan Senapati. "Thermal enhancement study of a transverse inverted-T shaped ribbed solar air heater." *International Communications in Heat and Mass Transfer* 119 (2020): 104922. https://doi.org/10.1016/j.icheatmasstransfer.2020.104922.

[16] Mahanand, Yadaba, and Jnana Ranjan Senapati. "Thermo-fluid analysis of a pentagonal ribbed triangular solar air heater duct (TSAHD): A three-dimensional numerical investigation." *International Communications in Heat and Mass Transfer* 137 (2022): 106258. https://doi.org/10.1016/j.icheatmasstransfer.2022.106258.

[17] Hai, Doan Thi Hong, and Nguyen Minh Phu. "A critical review of all mathematical models developed for solar air heater analysis." *Journal of Advanced Research in Fluid Mechanics and Thermal Sciences* 105, no. 1 (2023): 1-14. https://doi.org/10.37934/arfmts.105.1.114

[18] Yadav, Anil Singh, and Sanjay Kr Sharma. "Numerical simulation of ribbed solar air heater." In *Advances in Fluid and Thermal Engineering: Select Proceedings of FLAME 2020*, pp. 549-558. Springer Singapore, 2021. https://doi.org/10.1007/978-981-16-0159-0_49

[19] Yadav, Anil Singh, Mayank Kumar Dwivedi, Abhishek Sharma, and Vimal Kumar Chouksey. "CFD based heat transfer correlation for ribbed solar air heater." *Materials Today: Proceedings* 62 (2022): 1402-1407. https://doi.org/10.1016/j.matpr.2021.12.382.

[20] Chokphoemphun, Susama, Somporn Hongkong, Sanhawat Thongdaeng, and Suriya Chokphoemphun. "Experimental study and neural networks prediction on thermal performance assessment of grooved channel air heater." *International Journal of Heat and Mass Transfer* 163 (2020): 120397. https://doi.org/10.1016/j.ijheatmasstransfer.2020.120397.

[21] Kumar, Raj, Muneesh Sethi, Ranchan Chauhan, and Anil Kumar. "Experimental study of enhancement of heat transfer and pressure drop in a solar air channel with discretized broken V-pattern baffle." *Renewable Energy* 101 (2017): 856-872. https://doi.org/10.1016/j.renene.2016.09.033.